



1 Delineating wetland catchments and modeling hydrologic 2 connectivity using LiDAR data and aerial imagery

3 Qiusheng Wu¹, Charles R. Lane²

4 ¹Department of Geography, Binghamton University, State University of New York, Binghamton, NY 13902, USA

5 ²U.S. Environmental Protection Agency, Office of Research and Development, National Exposure Research
6 Laboratory, 26 W. Martin Luther King Dr., Cincinnati, OH 45268, USA

7 *Correspondence to:* Qiusheng Wu (wqs@binghamton.edu)

8 **Abstract:** In traditional watershed delineation and topographic modeling, surface depressions are generally treated
9 as spurious features and simply removed from a digital elevation model (DEM) to enforce flow continuity of water
10 across the topographic surface to the watershed outlets. In reality, however, many depressions in the DEM are actual
11 wetland landscape features that are seldom fully filled with water. For instance, wetland depressions in the Prairie
12 Pothole Region (PPR) are seasonally to permanently flooded wetlands characterized by nested hierarchical
13 structures with dynamic filling-spilling-merging surface-water hydrological processes. The objectives of this study
14 were to delineate hierarchical wetland catchments and model their hydrologic connectivity using high-resolution
15 LiDAR data and aerial imagery. The graph theory-based contour tree method was used to delineate the hierarchical
16 wetland catchments and characterize their geometric and topological properties. Potential hydrologic connectivity
17 between wetlands and streams were simulated using the least-cost path algorithm. The resulting flow network
18 delineated putative temporary or seasonal flow paths connecting wetland depressions to each other or to the river
19 network at scales finer than available through the National Hydrography Dataset. The results demonstrated that our
20 proposed framework is promising for improving overland flow simulation and hydrologic connectivity analysis.

21 **Keywords:** hydrologic connectivity, prairie pothole, wetland depressions, geographically isolated wetlands, flow
22 path, LiDAR

23 1 Introduction

24 The Prairie Pothole Region (PPR) of North America extends from the north-central United States to south-central
25 Canada, encompassing a vast area of approximately 720,000 km². The landscape of the PPR is dotted with millions
26 of wetland depressions formed by the glacial retreat that happened during the Pleistocene Epoch (Winter, 1989). The
27 PPR is considered as one of the largest and highly productive wetland areas in the world as it serves as a primary
28 breeding habitat for North America's waterfowl population (Keddy, 2010; Steen et al., 2014; Rover and Mushet,
29 2015). The wetland depressions, commonly known as potholes, possess important hydrological and ecological
30 functions, such as providing critical habitat for many migrating and breeding waterbirds (Minke, 2009), acting as
31 nutrient sinks (Oslund et al., 2010), and storing surface water that can attenuate peak runoff during a flood event
32 (Huang et al., 2011b). The pothole size ranges from a relatively small area of less than 100 m² to as large as 30,000



33 m², with an estimated median size of 1600 m² (Zhang et al., 2009; Huang et al., 2011a). Most potholes have a water
34 depth of less than 1 m with varying water permanency, ranging from ephemeral to permanent (Sloan, 1972). Due to
35 their small size and shallow depth, these wetlands are highly sensitive to climate variability and are vulnerable to
36 ecological, hydrological, and anthropogenic changes. Wetland depressions have been extensively drained and filled
37 due to agricultural expansion, which is considered as the greatest source of wetland loss in the PPR (Johnston,
38 2013). In a report to the United States (U.S.) Congress on the status of wetland resources, Dahl (1990) estimated that
39 the coterminous U.S. lost more than 50 percent of their original wetlands over a period of 200 years between the
40 1780s and the 1980s. More recently, Dahl (2014) reported that the total wetland area in the PPR declined by
41 approximately 300 km² between 1997 and 2009. This represents an average annual net loss of 25 km². Regarding
42 the number of depressions, it was estimated that the wetland depressions declined by over 107,000 or four percent
43 between 1997 and 2009 (Dahl, 2014).

44 The extensive wetland drainage and removal have increased precipitation runoff into regional river basins,
45 which is partially responsible for the increasing frequency and intensity of flooding events in the PPR (Miller and
46 Nudds, 1996; Bengtson and Padmanabhan, 1999; Todhunter and Rundquist, 2004). Concerns over flooding along
47 rivers in the PPR have stimulated the development of hydrologic models to simulate the effects of depression
48 storage on peak river flows (Hubbard and Linder, 1986; Gleason et al., 2007; Gleason et al., 2008; Huang et al.,
49 2011b). Since most of these prairie wetlands do not have surface outlets or well-defined surface water connections,
50 they are generally considered as geographically isolated wetlands (GIWs) (Tiner, 2003; Cohen et al., 2016; Lane and
51 D'Amico, 2016). Recently, the U.S. Environmental Protection Agency conducted a comprehensive review of over
52 1350 peer-reviewed papers with the aim to synthesize existing scientific understanding of how wetlands and streams
53 affect the physical, chemical, and biological integrity of downstream waters (U.S. EPA, 2015). The report concludes
54 that additional research focused on the frequency, magnitude, timing, duration, and rate of fluxes from GIWs to
55 downstream waters is needed to better identify wetlands with functions that significantly affect other waters and
56 maintain the long-term sustainability and resiliency of valued water resources (Rains et al., 2016).

57 In addition to the comprehensive review by the U.S. EPA (2015), a number of recent studies focusing on the
58 hydrologic connectivity of prairie wetlands have been reported in the literature. For example, Chu (2015) proposed a
59 puddle-to-puddle modeling framework to delineate prairie wetlands and characterize their dynamic hydro-
60 topographic properties in the Cottonwood Lake area (2.55 km²) using a 10-m resolution digital elevation model
61 (DEM). Vanderhoof et al. (2016) examined the effects of wetland expansion and contraction on surface water
62 connectivity in the PPR using time series Landsat imagery. Ameli and Creed (2016) developed a physically-based
63 hydrologic model to characterize surface and groundwater hydrologic connectivity of prairie wetlands. In a
64 comprehensive overview of wetland hydrology in the PPR, Hayashi et al. (2016) highlighted that prairie wetlands
65 and catchments should be considered as highly integrated hydrological units because the existence of prairie
66 wetlands depends on lateral inputs of runoff water from their catchments in addition to direct precipitation. To our
67 knowledge, however, few studies on the hydrology of prairie wetlands have treated wetlands and catchments as
68 integrated hydrological units. Furthermore, high-resolution light detection and ranging (LiDAR) data have rarely



69 been used in broad-scale (e.g., basin- or subbasin-scale) studies to delineate wetland catchments and model wetland
70 connectivity in the PPR.

71 In this paper, we present a semi-automated framework for delineating nested hierarchical wetland
72 depressions and their corresponding catchments as well as simulating wetland connectivity using high-resolution
73 LiDAR data. The hierarchical structure of wetland depressions and catchments was identified and quantified using
74 the localized contour tree method (Wu et al., 2015). The potential hydrologic connectivity between wetlands and
75 streams was characterized using the least-cost path algorithm. The resulting flow network delineated putative
76 temporary or seasonal flow paths connecting wetland depressions to each other or to the river network at scales finer
77 than available through the National Hydrography Dataset. The results demonstrated that our proposed framework is
78 promising for improving overland flow simulation and hydrologic connectivity analysis, which subsequently may
79 improve the understanding of wetland hydrological dynamics at watershed scales.

80 **2 Study area and datasets**

81 **2.1 Study area**

82 Our study area focused on the Pipestem River subbasin in the Prairie Pothole Region of North Dakota (Fig. 1). The
83 subbasin is an 8-digit Hydrologic Unit Code (#10160002) with a total area of approximately 2,770 km², covering
84 four counties in North Dakota (see Fig. 1). The climate of the subbasin is characterized by long, cold, dry winters
85 and short, mild, variably wet summers (Winter and Rosenberry, 1995). Average annual precipitation is
86 approximately 440 mm with substantial seasonal and annual variations (Huang et al., 2011a). The land cover of the
87 Pipestem subbasin is dominated by cultivated crops (44.1%), herbaceous vegetation (25.9%), and pay/pasture
88 (13.1%), with a substantial amount of open water (7.1%) and emergent herbaceous wetlands (5.6%) (Jin et al.,
89 2013). The Cottonwood Lake area (see the blue rectangle in Fig. 1), a long-term field research site established by the
90 U.S. Geological Survey (USGS) and the U.S. Fish and Wildlife Service (USFWS) in 1977 for wetland ecosystem
91 monitoring, has been a very active area of research for several decades (e.g., Sloan, 1972; Winter and Rosenberry,
92 1995; Huang et al., 2011a; Mushet and Euliss, 2012; Hayashi et al., 2016).

93 **2.2 LiDAR data**

94 The LiDAR elevation data for the Pipestem subbasin were collected in the late October of 2011 and distributed
95 through the North Dakota GIS Hub Data Portal (<https://gis.nd.gov/>, accessed December 30, 2016). The bare-earth
96 digital elevation models (DEMs) derived from LiDAR point clouds are freely available as 1-m resolution image tiles
97 (2 km × 2 km). The vertical accuracy of the LiDAR DEM is 15.0 cm. In total, the Pipestem Subbasin consists of 786
98 DEM tiles with an aggregated file size of 22.66 GB. We created a seamless LiDAR DEM (see Fig. 1) for the
99 Pipestem subbasin by mosaicking 786 DEM tiles and used it for all subsequent data analyses. The elevation of the
100 subbasin ranges from 422 m to 666 m, with relatively high-elevation areas in the west and low-elevation areas in the
101 east.



102 The LiDAR intensity data for the Pipestem subbasin were also collected at 1-m resolution coincident with
103 the LiDAR elevation data collection. In general, the return signal intensities of water areas are relatively weak due to
104 water absorption of the near-infrared spectrum (Lang and McCarty, 2009; McCauley and Anteau, 2014). As a result,
105 waterbodies typically appear as dark features whereas non-water areas appear as relatively bright features in the
106 LiDAR intensity image. Thresholding techniques have been commonly used to distinguish water pixels from non-
107 water pixels (Huang et al., 2011b; Huang et al., 2014; Wu and Lane, 2016). In this study, the LiDAR intensity data
108 were primarily used to extract standing-water areas (i.e., inundation areas) while the LiDAR DEMs were used to
109 derive nested wetland depressions and their corresponding catchments above the standing-water surface.

110 **2.3 Ancillary data**

111 In addition to the LiDAR datasets, we used three ancillary datasets, including the 1-m resolution aerial imagery from
112 the National Agriculture Imagery Program (NAIP) of the U.S. Department of Agriculture (USDA), National
113 Wetlands Inventory (NWI) from the USFWS, and National Hydrography Dataset (NHD) from the USGS.

114 The NAIP imagery products were also acquired from the North Dakota GIS Hub Data Portal. The default
115 spectral resolution of the NAIP imagery in North Dakota is natural color (Red, Green, and Blue, or RGB).
116 Beginning in 2007, however, the state has been delivered with four bands of data: RGB and Near Infrared. We
117 downloaded and processed six years of NAIP imagery for the Pipestem subbasin, including 2003, 2004, 2006, 2009,
118 2012, and 2014. A small portion of the study area with the NAIP imagery is shown in Fig. 2. These time-series
119 NAIP imagery clearly demonstrate the dynamic nature of prairie pothole wetlands under various dry and wet
120 conditions. In particular, the extremely wet year of 2014 resulted in many individual wetlands to coalesce and form
121 larger wetland complexes (see the yellow arrows in Fig. 2). It should be noted that all the NAIP imagery were
122 collected during the summer growing season of agricultural crops. Since no coincident aerial photographs were
123 collected during the LiDAR data acquisition campaign in 2011, these NAIP imagery can serve as valuable data
124 sources for validating the LiDAR-derived wetlands catchments and hydrological pathways in this study.

125 The NWI data for our study area were downloaded from <https://www.fws.gov/wetlands/> (accessed
126 December 30, 2016). These wetlands inventory data in this region were created by manually interpreting aerial
127 photographs acquired in the 1980s with additional support from soil surveys and field checking (Cowardin et al.,
128 1979; Huang et al., 2011b; Wu and Lane, 2016). Tiner (1997) reported that the target mapping unit, the size class of
129 the smallest group of NWI wetlands that can be consistently mapped, was between 1000 m² and 4000 m² in the
130 Prairie Pothole Region. It should be noted that the target mapping unit is not the minimum wetland size of the NWI.
131 In fact, there are a considerable amount of NWI wetland polygons smaller than the target mapping unit (1000 m²). In
132 this study, we focused on the prairie wetlands that are greater than 500 m². Therefore, 5644 small NWI wetland
133 polygons (< 500 m²) were eliminated from further analysis. In total, there were 32,016 NWI wetland polygons (≥
134 500 m²) across the Pipestem subbasin (Table 1). The total size of these NWI wetlands was approximately 279.5 km²,
135 covering 10.1% of the Pipestem subbasin. The areal composition of NWI wetlands were freshwater emergent
136 wetlands (86.5%), lakes (7.5%), freshwater ponds (5.3%), freshwater forested/shrub wetland (0.4%), and riverine
137 systems (0.3%). The median size of wetlands (≥ 500 m²) in our study area was 1778 m². Although the NWI data is



138 the only spatially comprehensive wetland inventory for our study area, it is now considerably out-of-date, as it was
139 developed 30 years ago and it does not reflect the wetland temporal change (Johnston, 2013). The wetland extent
140 and type for many wetland patches have changed since its original delineation (e.g., Fig. 2). Nevertheless, NWI does
141 provide valuable information about wetland locations (Tiner, 1997; Huang et al., 2011b). In our study, the NWI
142 polygons were primarily used to compare with the wetland depressions delineated from the LiDAR DEM.

143 The NHD data were downloaded from <http://nhd.usgs.gov> (accessed December 30, 2016). There were 1840
144 polyline features in the NHD flowline layer for the Pipestem subbasin, with a total length of 1402.2 km and an
145 average length of 762.1 m. The NHD flowlines overlaid on top of the LiDAR DEM with is shown in Fig. 1. It is
146 worth noting that the majority of the NHD flowline features were found in the low-elevation areas in the east. The
147 high-elevation areas in the west where most NWI wetland polygons are located have very few NHD flowlines,
148 except for the Little Pipestem Creek. This implies that a large number of temporary and seasonal flow paths were
149 not captured in the NHD dataset. It is also worth noting that the NHD does not try to systematically measure stream
150 lines <1.6 km (Stanislowski, 2009; Lane and D'Amico, 2016). In this study, the NHD flowlines were used to
151 compare the LiDAR-derived flow paths using our proposed methodology.

152 **3 Methodology**

153 **3.1 Outline**

154 Our methodology for delineating nested wetland catchments and flow paths is a semi-automated approach consisting
155 of several key steps: (a) extraction of hierarchical wetland depressions using the localized contour tree method (Wu
156 et al., 2015); (b) delineation of nested wetland catchments; (c) calculation of potential water storage; and (d)
157 derivation of flow paths using the least-cost path search algorithm. The LiDAR DEM is used to delineate
158 hierarchical wetland depressions and nested wetland catchments. The LiDAR intensity imagery is used to extract
159 wetland inundation areas. The potential water storage of each individual wetland depression is calculated as the
160 volume between the standing water surface and the maximum water boundary where water may overflow into
161 downstream wetlands or waters. The flow paths representing surface water connectivity can then be derived
162 according to the potential water storage and simulated rainfall intensity. The flowchart in Fig. 3 shows the detailed
163 procedures of the methodology for delineating wetland catchments and flow paths.

164 **3.2 Extraction of hierarchical wetland depressions**

165 The fill-and-spill hydrology of prairie wetland depressions have received considerable attention in recent years
166 (Shaw et al., 2012; Shaw et al., 2013; Golden et al., 2014; Chu, 2015; Hayashi et al., 2016; Wu and Lane, 2016). It
167 is generally acknowledged that the fill-and-spill mechanism of wetland depressions results in intermittent hydrologic
168 connectivity between wetlands in the Prairie Pothole Region of North America. In this study, wetland depressions
169 were categorized into two groups based on their hierarchical structure: simple depressions and composite
170 depressions. A simple depression is a depression that does not have any other depressions embedded in it, whereas a
171 composite depression is composed of two or more simple depressions (Wu and Lane, 2016). As shown in Fig. 4(a),



172 for example, depressions A, B, C, D and E are all simple depressions. As water level gradually increases in these
173 simple depressions, they will eventually begin to spill and merge to form composite depressions. For instance, the
174 two adjacent simple depressions A and B can form a composite depression F (see Fig. 4(b)). Continuously,
175 composite depression F and simple depression C can further coalesce to form an even larger composite depression
176 G. Similarly, the two adjacent simple depressions D and E can coalesce to form a composite depression H.

177 It is worth noting that the flow direction of surface waters resulting from the fill-and-spill mechanism
178 between adjacent wetland depressions can be bidirectional, depending on the antecedent water level and potential
179 water storage capability of the depressions. Most previous studies simply assumed that water always flows
180 unidirectionally from an upper waterbody to a lower one. This assumption, however, does not apply when two
181 adjacent depressions share the same spilling elevation or when there is a groundwater hydraulic head preventing the
182 flow from one to another. For example, in Fig. 4(a), the water flow direction resulting from fill-and-spill between
183 depressions A and B can be bidirectional. If depression B fills up more quickly than depression A, then water will
184 flow from depression B to depression A through the spilling point, and vice versa. Depression with a high elevation
185 of antecedent water level does not necessarily spill to an adjacent depression with a lower elevation of antecedent
186 water level. The key factors affecting the initialization of spilling process leading to flow direction are the
187 depression ponding time and catchment precipitation conditions. If the rain or runoff comes from the east and that is
188 where depression B is, then it might fill more quickly than if the runoff comes from the west where depression A is.
189 The wetland depression whichever takes less time to fill up will spill to the adjacent depression and eventually
190 coalesce to form a larger composite depression. If no adjacent depression with the same spilling elevation is
191 available, the upstream wetland depression will directly spill to downstream wetlands or river streams. For example,
192 the largest fully-filled composite depression G will spill to the simple depression D or the composite depression H, if
193 available.

194 To identify and delineate the nested hierarchical structure of potential wetland depressions, we utilized the
195 localized contour tree method proposed by Wu et al. (2015). The concept of contour tree was initially proposed to
196 extract key topographic features (e.g., peaks, pits, ravines, and ridges) from contour maps (Kweon and Kanade,
197 1994). The contour tree is a tree data structure that can represent the nesting of contour lines on a continuous
198 topographic surface. Wu et al. (2015) improved and implemented the contour tree algorithm, making it a locally
199 adaptive version. In other words, the localized contour tree algorithm builds a series of trees rather than a single
200 global contour tree for the entire area. Each localized contour tree represents one disjointed depression (simple or
201 composite), and the number of trees represents the total number of disjointed depressions for the entire area. When a
202 disjointed depression is fully flooded, the water in it will spill to the downstream wetlands or waters through
203 overland flow. For example, Fig. 4(c) and (d) show the corresponding contour tree graphs for the composite
204 depressions in Fig. 4(b). Once the composite depression G is fully filled, water will spill into simple depression D or
205 composite depression H.

206 3.3 Delineation of nested wetland catchments



207 After the identification and extraction of hierarchical wetland depressions from the contour maps, various
208 hydrologically relevant terrain attributes can be derived based on the DEM, including flow direction, flow
209 accumulation, catchment boundary, flow path, flow length, etc. The calculation of flow direction is essential in
210 hydrological analysis because it frequently serves as the first step to derive other hydrologically important terrain
211 attributes. On a topographic surface represented in a DEM, flow direction is the direction of flow from each grid cell
212 to its steepest downslope neighbor. One of the widely used flow direction algorithms is the eight-direction flow
213 model known as the D8 algorithm (O'Callaghan and Mark, 1984), which is available in most GIS software packages.
214 Flow accumulation is computed based on flow direction. Each cell value in the flow accumulation raster represents
215 the number upslope cells that flow into it. In general, cells with high flow accumulation values correspond to areas
216 of concentrated flow (e.g. stream channels), while cells with a flow accumulation value of zero correspond to the
217 pattern of ridges (Zhu, 2016). Therefore, flow accumulation provides a basis for identifying ridgelines and
218 delineating catchment boundaries.

219 A catchment is the upslope area that drains water to a common outlet. It is also known as the watershed,
220 drainage basin, or contributing area. Catchment boundaries can be delineated from a DEM by identifying ridgelines
221 between catchments based on a specific set of catchment outlets (i.e., spilling points). In traditional hydrological
222 modeling, topographic depressions are commonly treated as spurious depressions (or is it “features”) and simply
223 removed to create a hydrologically correct DEM, which enforces water to flow continuously across the landscape to
224 the catchment outlets (e.g., stream gauges, dams). In the PPR, however, most topographic depressions in the DEM
225 are real features that represent wetland depressions, which are rarely under fully-filled condition (see Hayashi et al.,
226 2016; Lane and D'Amico, 2016; Vanderhoof et al., 2016). As illustrated above, we use the localized contour tree
227 algorithm to delineate the hierarchical wetland depressions, which can be used as the source locations for delineating
228 wetland catchments. Each wetland depression (simple or composite) has a corresponding wetland catchment. As
229 shown in Fig. 4(b), the corresponding wetland catchment of each wetland depression is bounded by the vertical lines
230 surrounding that depression. For example, the wetland catchment of simple depression A is $Catchment_{tm}$, and the
231 wetland catchment of simple depression B is $Catchment_{mn}$. Similarly, the wetland catchment of composite
232 depression F is $Catchment_{tm}$, which is an aggregated area of $Catchment_{tm}$ and $Catchment_{mn}$, resulting from the
233 coalesce from simple depressions A and B.

234 3.4 Calculation of water storage and ponding time

235 The potential water storage capacity (V [m^3]) of each wetland depression can be computed through statistical
236 analysis of the grid cells that fall within the depression (Wu and Lane, 2016):

237

$$V = \sum_{i=1}^n (C - Z_i) \cdot R^2 \quad (1)$$



238 where C is the spilling elevation (m), i.e., the elevation of the grid cell where water spills out of the depression; Z_i
239 is the elevation of the grid cell i (m); R is the spatial resolution (m); and n is the total number of grid cells that fall
240 within the depression.

241 The ponding time of a depression can be calculated as follows:

$$242 \quad T = V / (A_c \cdot I) \cdot 1000 \quad (2)$$

243 where V is the potential water storage capacity of the depression (m^3); A_c is the catchment area of the
244 corresponding depression (m^2); and I is the rainfall intensity (mm/h). For the sake of simplicity, we assume that the
245 rainfall is temporally and spatially consistent and uniformly distributed throughout the landscape and all surfaces are
246 impervious.

247 The proportion of wetland depression area (A_w) to catchment area (A_c) is calculated by:

$$248 \quad P_{wc} = A_w / A_c \quad (3)$$

249 The wetland depression area (A_w) refers to the maximum ponding extent of the depression. The proportion (P_{wc})
250 can serve as a good indicator for percent inundation of the study area under extremely wet conditions (e.g.,
251 Vanderhoof et al., 2016).

252 **3.5 Derivation of surface-water flow paths**

253 Based on the computed ponding time of each depression under a specific rainfall intensity, the most probable
254 sequence of the overland flow path can be constructed. The depression with the least ponding time will first fill and
255 start to overspill down-gradient. In hydrology, the path which water takes to travel from the spilling point to the
256 downstream surface outlet or channel is commonly known as flow path. The distance it takes for water to travel is
257 known as flow length. In this study, we adopted and adapted the least-cost path search algorithm (Wang and Liu,
258 2006; Metz et al., 2011; Stein et al., 2011) to derive the potential flow paths. The least cost path algorithm requires
259 two input datasets: the DEM and the depression polygons. Given the fact that topographic depressions in high-
260 resolution LiDAR DEM are frequently a combination of artifacts and actual landscape features (Lindsay and Creed,
261 2006), the user can set a minimum size threshold for depressions to be treated as actual landscape features. In other
262 words, depressions with a size smaller than the threshold will be treated as artifacts, and thus removed from the
263 DEM. This results in a partially-filled DEM in which depressions smaller than the chosen threshold are filled to
264 enforce hydrologic flow while larger depressions are kept for further analysis. Based on the partially-filled DEM,
265 flow direction for each grid cell can be calculated using the D8 flow direction algorithm (O'Callaghan and Mark,
266 1984). The least cost path minimizes the cumulative cost (i.e., elevation) along its length. Flow paths are computed
267 by tracing down gradient, from higher to lower cells, following assigned flow directions. With the simulated
268 overland flow path, flow length can be calculated, which is defined as the distance between the spilling point of an
269 upslope wetland and the inlet of a downslope wetland or stream. In our study, hydrologic connectivity refers to the
270 water movement between wetland-wetland and wetland-stream via hydrologic pathways of surface water.



271 3.6 Wetland Hydrology Analyst

272 To facilitate automated delineation of wetland catchments and flow paths, we have implemented the proposed
273 framework as an ArcGIS toolbox – Wetland Hydrology Analyst, which is freely available for download at
274 <https://GISTools.github.io/> (accessed December 30, 2016). The core algorithms of the toolbox were implemented
275 using the Python programming language. The toolbox consists of three tools: Wetland Depression Tool, Wetland
276 Catchment Tool, and Flow Path Tool. The Wetland Depression Tool asks the user to select a DEM grid, and then
277 executes the localized contour tree algorithm with user-defined parameters (e.g., base contour elevation, contour
278 interval, min. depression size, min. ponding depth) automatically to delineate hierarchical wetland depressions. The
279 depressional wetland polygons can be stored as ESRI Shapefiles or a Feature Dataset in a Geodatabase. Various
280 morphometric properties (e.g., width, length, size, perimeter, max. depth, mean depth, volume, elongatedness,
281 compactness) are computed and included in the attribute table of the wetland polygon layers. The Wetland
282 Catchment Tool uses the DEM grid and the wetland polygon layers resulted from the Wetland Depression Tool as
283 input, and exports wetland catchment layers in both vector and raster format. The Flow Path Tool can be used to
284 derive overland flow path of surface water based on the DEM grid and the wetland polygon layers.

285 4 Results

286 4.1 Inundation mapping

287 The LiDAR intensity image was primarily used to map inundation areas. Before inundation mapping, we applied a
288 median filter to smooth the LiDAR intensity image. The median filter is considered as an edge-preserving filter that
289 can effectively remove data noise while preserving boundaries between image objects (Wu et al., 2014).
290 Subsequently, a simple thresholding method was used to separate inundated and non-inundated classes. Similar
291 thresholding techniques have been used in previous studies to extract water areas from LiDAR intensity imagery
292 (Lang and McCarty, 2009; Huang et al., 2011b). By examining typical inundation areas and the histogram of the
293 LiDAR intensity imagery used in our study, we chose an intensity threshold value of 20. Grid cells with an intensity
294 value between 0 and 20 were classified as an inundated class while grid cells with an intensity value greater than 20
295 as a non-inundated class, which resulted in a binary image. In the binary image, each region composed of inundated
296 pixels that were spatially connected (8-neighbor) was referred to as a potential inundation object. The “boundary
297 clean” and “region group” functions in ArcGIS Spatial Analyst were then used to clean ragged edges of the potential
298 inundation objects and assign a unique number to each object. It should be noted that water and live trees might both
299 appear as dark features in the LiDAR intensity imagery and have similar intensity values, although trees are not
300 particularly common in this region. As a result, some trees were misclassified as inundation objects. To correct the
301 misclassifications and obtain reliable inundation objects, we further refined the potential inundation objects using
302 additional criteria with the aid of the LiDAR DEM. First of all, we assumed that each inundation object must occur
303 within a topographic depression in order to retain water. In other words, all inundation objects must intersect with
304 depression objects derived using the “sink” function in ArcGIS Spatial Analyst. Secondly, given the relatively flat
305 and level surface of inundated regions, the standard deviation of pixel elevations within the same inundation object



306 should be very small. By examining the standard deviation of pixel elevations of some typical inundation objects
307 and tree objects, we chose a threshold of 0.25 m, which is slightly larger than the vertical accuracy of the LiDAR
308 data (0.15 m). This step can be achieved using the “zonal statistics as table” in ArcGIS Spatial Analyst. Thirdly, we
309 only focused on wetlands greater than 500 m². Therefore, inundation objects with areas smaller than 500 m² were
310 eliminated from further analysis.

311 Using the above procedures, we identified 15,784 inundation objects (i.e., depressions ≥ 500 m² with water
312 as determined through LiDAR-based analyses), which were then compared against the NWI wetland polygons in
313 our study area. We have made the inundation map publicly available at <https://GISTools.github.io/> (accessed
314 December 30, 2016). The identified inundation objects encompassed an area of approximately 278.5 km²,
315 accounting for 10.1 % of the Pipestem subbasin. Using the empirical area-to-volume equation developed for this
316 region of the PPR (see Gleason et al., 2007; Wu and Lane, 2016), we estimated that the 15,784 inundated
317 depressions stored approximately 448.5 million m³ of water. The histogram of inundation polygons is shown in Fig.
318 5(a). The median size of the inundation polygons identified using the LiDAR intensity data was 1828 m², which was
319 slightly larger than the reported median size of NWI polygons (Table 2). Surprisingly, 18,957 out of 32,016 NWI
320 wetland polygons did not intersect with the inundation objects. In other words, 59.2% of the NWI wetland polygons
321 mapped in the 1980s were found to be partly or completely dried out or destroyed during the LiDAR collection
322 period. The total area of these dried NWI wetlands were 43.6 km², accounting for 15.6% of the original NWI
323 wetland areas (279.5 km²). The histogram of the dried NWI wetlands is shown in Fig. 5(b). It is worth noting that
324 most dried NWI wetlands were relatively small with a median size of 1212 m² (Table 2). The LiDAR intensity data
325 were acquired in late October 2011, an extremely wet month according to the Palmer Hydrological Drought Index
326 (Fig. 6). During this wet season, most wetlands would be expected to have abundant standing water. If no standing
327 water could be detected in a wetland patch during this extremely wet period, we can safely conclude that the wetland
328 patch had probably dried out during the past decades, although we could not infer the exact time when it occurred.
329 The ‘dried’ NWI wetlands could also be attributed to the source of error in the original NWI data, which has a
330 minimum mapping unit (i.e., the minimum sized wetland that can be consistently mapped) of 0.1 ha for the PPR
331 (Tiner, 1997). Figure 5(b) shows that 37% of the ‘dried’ NWI polygons are smaller than the minimum mapping unit
332 (1000 m²). This implies that these small ‘dried’ NWI polygons could be due to the NWI mapping error. Figure 7
333 illustrates the difference in shape and extent between the LiDAR-derived wetland inundation maps and the NWI
334 wetland polygons. The areas of disagreement (discrepancy) can be partly explained by the different image
335 acquisition dates. As mentioned earlier, the NWI maps for Pipestem subbasin of the PPR were created in the early
336 1980s while the LiDAR data were acquired in 2011. Clearly, most small NWI wetlands (see blue-outline polygons
337 in Fig. 7) appeared to not have visible standing water. Conversely, large NWI wetlands exhibited expansion and
338 coalesced to form even large wetland complexes (see yellow-outline polygons in Fig. 7).

339 4.2 Nested wetland depressions and catchments

340 We applied the localized contour method on the LiDAR-derived DEM and identified 33,241 wetland depressions. It
341 should be noted that the ‘wetland depression’ refers to the maximum potential ponding extent of the depression. The



342 inundated wetland depressions identified in the prior section can be seen as a subset of these depressions with water
343 in them. The total area of the identified wetland depressions was approximately 554.5 km² (Table 3), accounting for
344 20% of the entire study area. This histogram of the wetland depressions is shown in Fig. 8(a). The median size of
345 wetland depressions was 2592 m², which is larger than that of the NWI wetland polygons as well as the inundation
346 polygons (see Table 2). Using Eq. (1), we estimated that the potential water storage capacity of the Pipestem
347 subbasin resulting from these wetland depressions is 782.8 million m³, which is 1.75 times as large as the estimated
348 existing water storage (448.5 million m³) for the 15,784 inundated wetlands mentioned above. As noted by Hayashi
349 et al. (2016), wetlands and catchments are highly correlated and should be considered as integrated hydrological
350 units. The water input of each wetland largely depends on runoff from the upland areas within the catchment. Using
351 the method described in Section 3.3, we delineated the associated wetland catchments for each of the 33,241
352 wetland depressions. The histogram of the delineated wetland catchments is shown in Fig. 8(b). The median size of
353 wetland catchments was 25,780 m², which is approximately ten times larger than that of the wetland depressions
354 (Table 3).

355 Using Eq. (3), we calculated the proportion of depression area to catchment area (A_w / A_c) for each wetland
356 depression. It was found that the proportion ranged from 0.04% to 83.72%, with a median of 14.31% (Table 3). Our
357 findings are in general agreement with previous studies (Hayashi et al., 2016). For instance, Hayashi et al. (1998)
358 reported an average proportion (A_w / A_c) of 9% for 12 prairie wetlands in the Canadian portion of the PPR.
359 Similarly, Watmough and Schmoll (2007) analyzed 13 wetlands in the Cottonwood Lake Area during the high-stage
360 period and reported an average proportion (A_w / A_c) of 18%. It should be noted that the average proportion of
361 wetland area to catchment area (A_w / A_c) reported in the above studies were calculated on the basis of a limited
362 number of wetlands. On the contrary, our results were computed from more than 30,000 wetland depressions and
363 catchments, which provides a statistically reliable result due to a much larger sample size.

364 4.3 Flow paths and connectivity lengths

365 Based on the LiDAR DEM and wetland depression polygon layer, we derived the complete flow path network for
366 our study area using the least-cost path algorithm. We have made the interactive map of hydrologic connectivity in
367 the Pipestem subbasin publicly available at <https://GISTools.github.io/> (accessed December 30, 2016). A number of
368 data layers derived from our study are available on the map, such as the inundation polygons, wetland depressions,
369 wetland catchments, and flow paths. NWI polygons, NHD flowlines, LiDAR intensity image, LiDAR shaded relief,
370 and time-series aerial photographs are also available for results comparison and visualization. A small proportion of
371 the map is shown in Fig. 9. Clearly, the derived flow paths not only captured the permanent surface water flow paths
372 (see the thick blue NHD flowline in Fig. 9), but also the intermittent and infrequent flow paths that have not been
373 mapped previously. By examining the potential flow paths overlaid on the color infrared aerial photograph (Fig.
374 9(b)), we can see that the majority of flow paths appeared to be collocated with vegetated areas. This indicates that
375 flow paths are likely located in high soil moisture areas that are directly or indirectly related to surface water or
376 groundwater connectivity.



377 In total, there are 1840 NHD flowlines in the Pipestem subbasin. The mean and median length of NHD
378 flowlines are 762 m and 316 m, respectively (Table 4). However, the flow lengths derived from our study, which
379 connected not only stream segments but also wetlands to wetlands, revealed much shorter flow paths than the NHD
380 flowlines. This finding is within our expectation. The histogram of the derived flow lengths is shown in Fig. 10. The
381 median flow length is 83 m, which is approximately 1/4 of the median NHD flowlines. The median elevation
382 difference between an upstream wetland and a downstream wetland connected through the flow path is 0.89 m.

383 5 Discussion

384 It should be noted that the LiDAR data we used in this study were collected in the late October of 2011, which was
385 an extremely wet period according to the Palmer Hydrological Drought Index (see Fig. 6). During such wet period,
386 most wetlands exhibited high water levels and large water extents, which can be evidenced from the LiDAR
387 intensity image in Fig. 7 and the aerial photograph in Fig. 9. It can be clearly seen that most wetlands, particularly
388 those larger ones, appeared to have larger water extents compared to the NWI polygons. A substantial number of
389 NWI wetlands were found inundated to coalesce with adjacent wetlands and form larger wetland complexes. LiDAR
390 data acquired during high water levels is desirable for studying maximum water extents of prairie wetlands.
391 However, the use of wet-period LiDAR data alone is not ideal for studying the fill-and-spill hydrology of prairie
392 wetlands. Since LiDAR sensors working in the near-infrared spectrum typically could not penetrate water, it is
393 impractical to derive bathymetric information of the depression. As a result, the delineation and characterization of
394 individual wetland depressions nested within larger inundated wetland complexes were not possible. Bathymetric
395 LiDAR systems with a green laser onboard offer a promising solution for acquiring wetland basin morphometry due
396 to the higher penetration capability of the green laser (Wang and Philpot, 2007). In addition, the derivation of
397 antecedent water depth and volume of wetland depressions is difficult, which can only be estimated using empirical
398 equations based on the statistical relationship between depression area and depression volume (Hayashi and Van der
399 Kamp, 2000; Gleason et al., 2007). As noted earlier, the volume of water in the 15,784 inundated wetlands was
400 estimated to be 448.5 million m³. Ideally, using multiple LiDAR datasets acquired in both dry and deluge conditions
401 in conjunction with time-series aerial photographs would be essential for studying the fill-and-spill mechanism of
402 prairie wetlands. In this case, we can use the dry-period LiDAR data to delineate and characterize the morphology of
403 individual wetland depressions before the fill-and-spill processes occur. Furthermore, we can derive the potential
404 flow paths and project the coalescing of wetland depressions after the fill-and-spill processes initiate. The wet-
405 period LiDAR data and time-series aerial photographs can serve as validation datasets to evaluate the fill-and-spill
406 patterns.

407 It is also worth noting that the proposed methodology in this study was designed to reflect the topography
408 and hydrologic connectivity between wetlands in the Prairie Pothole Region. We have made assumptions to simplify
409 the complex prairie hydrology. Physically-based hydrological models (e.g., Brunner and Simmons, 2012; Ameli and
410 Creed, 2016) have not yet been integrated into our framework. However, fill-and-spill is a complex and spatially
411 distributed hydrological process highly affected by many factors, such as surface topography, surface roughness, soil
412 infiltration, soil properties, depression storage, precipitation, evapotranspiration, snowmelt runoff, and groundwater



413 exchange (Tromp-van Meerveld and McDonnell, 2006a, b; Evenson et al., 2015; Zhao and Wu, 2015; Evenson et
414 al., 2016; Hayashi et al., 2016). Nevertheless, our study presents the first attempt to use LiDAR data for deriving
415 nested wetland catchments and simulating flow paths in the broad-scale Pipestem subbasin in the PPR. Previous
416 studies utilizing high-resolution digital elevation data (e.g., LiDAR, Interferometric Synthetic Aperture Radar
417 [IfSAR]) for studying prairie wetlands were mostly confined in small-scale areas (e.g., plot scale, small watershed
418 scale) with a limited number of wetlands, whereas broad-scale studies using physically-based hydrological models
419 have rarely used LiDAR data to delineate and characterize individual wetland depressions or catchments. Coupled
420 surface-subsurface flow models with hydrologic, biogeochemical, ecologic, and geographic perspectives have yet to
421 be developed for broad-scale studies in the PPR (Golden et al., 2014; Amado et al., 2016). Further efforts are still
422 needed to improve the understanding of the integrated surface-water and groundwater processes of prairie wetlands.

423 **6 Conclusions**

424 Accurate delineation and characterization of wetland depressions and catchments are essential for understanding the
425 hydrology of prairie wetlands. In this study, we accurately delineated the inundation areas while reducing the
426 confounding factor of live trees by using the LiDAR-derived DEM in conjunction with the coincident LiDAR
427 intensity imagery. In addition, we developed a semi-automated framework for identifying nested hierarchical
428 wetland depressions and delineating their corresponding catchments using the localized contour tree method.
429 Furthermore, we quantified the potential hydrologic connectivity between wetlands and streams based on the
430 overland flow networks derived using the least-cost path algorithm on LiDAR data. Although the results presented
431 in this study are specific to the Pipestem subbasin, the proposed framework can be easily adopted and adapted to
432 other PPR regions, as well as other wetland regions where fine-resolution LiDAR data are available. The new tools
433 that we developed for identifying hydrologic connectivity between wetlands and stream networks can better inform
434 wetland regulation debates and enhance the ability to better manage wetlands under various planning scenarios. The
435 resulting flow network delineated putative temporary or seasonal flow paths connecting wetland depressions to each
436 other or to the river network at scales finer than available through the National Hydrography Dataset. The results
437 demonstrated that our proposed framework is promising for improving overland flow modeling and hydrologic
438 connectivity analysis (Golden et al., 2016).

439 Broad-scale prairie wetland hydrology has been difficult to study with traditional remote sensing methods.
440 LiDAR-derived DEMs can be used to map hydrologic flow pathways, which regulate the ability of wetlands to
441 provide ecosystem services (Lang and McCarty, 2009). This study is an initial step towards the development of a
442 spatially distributed hydrologic model to fully describe the hydrologic processes in broad-scale prairie wetlands.
443 Additional field work and the integration of physically-based model of surface and subsurface process would benefit
444 the study. Importantly, the results capture temporary and ephemeral hydrologic connections and provide essential
445 information for wetland scientists and decision-makers to more effectively plan for current and future management
446 of prairie wetlands.

447



448 **Data and code availability**

449 The data and ArcGIS toolbox developed for this paper are available for download at <https://GISTools.github.io/>.

450 **Competing interests**

451 The authors declare that they have no conflict of interest.

452 **Disclaimer**

453 This paper has been reviewed in accordance with the U.S. Environmental Protection Agency's peer and
454 administrative review policies and approved for publication. Mention of trade names or commercial products does
455 not constitute endorsement or recommendation for use. Statements in this publication reflect the authors'
456 professional views and opinions and should not be construed to represent any determination or policy of the U.S.
457 Environmental Protection Agency.

458 **References**

- 459 Amado, A. A., Politano, M., Schilling, K., and Weber, L.: Investigating Hydrologic Connectivity of a Drained
460 Prairie Pothole Region Wetland Complex using a Fully Integrated, Physically-Based Model, *Wetlands*, 1-13,
461 10.1007/s13157-016-0800-5, 2016.
- 462 Ameli, A. A., and Creed, I. F.: Quantifying hydrologic connectivity of wetlands to surface water systems, *Hydrol.*
463 *Earth Syst. Sci. Discuss.*, 2016, 1-28, 10.5194/hess-2016-404, 2016.
- 464 Bengtson, M. L., and Padmanabhan, G.: A hydrologic model for assessing the influence of wetlands on flood
465 hydrographs in the Red River Basin: Development and application, Citeseer, 1999.
- 466 Brunner, P., and Simmons, C. T.: HydroGeoSphere: A Fully Integrated, Physically Based Hydrological Model,
467 *Ground Water*, 50, 170-176, 10.1111/j.1745-6584.2011.00882.x, 2012.
- 468 Chu, X.: Delineation of Pothole-Dominated Wetlands and Modeling of Their Threshold Behaviors, *Journal of*
469 *Hydrologic Engineering*, D5015003, 2015.
- 470 Cohen, M. J., Creed, I. F., Alexander, L., Basu, N. B., Calhoun, A. J., Craft, C., D'Amico, E., DeKeyser, E., Fowler,
471 L., and Golden, H. E.: Do geographically isolated wetlands influence landscape functions?, *Proceedings of the*
472 *National Academy of Sciences*, 113, 1978-1986, 2016.
- 473 Cowardin, L. M., Carter, V., Golet, F. C., and LaRoe, E. T.: Classification of wetlands and deepwater habitats of the
474 United States, U.S. Department of the Interior, Fish and Wildlife Service, Washington, D.C., 131, 1979.
- 475 Dahl, T. E.: Wetlands losses in the United States, 1780's to 1980's. Report to the Congress, U.S. Department of the
476 Interior, Fish and Wildlife Service, Washington, D.C., 13, 1990.
- 477 Dahl, T. E.: Status and trends of prairie wetlands in the United States 1997 to 2009, U.S. Department of the Interior,
478 Fish and Wildlife Service, Ecological Services, Washington, D.C., 67, 2014.
- 479 Evenson, G. R., Golden, H. E., Lane, C. R., and D'Amico, E.: Geographically isolated wetlands and watershed
480 hydrology: A modified model analysis, *Journal of Hydrology*, 529, Part 1, 240-256,
481 <http://dx.doi.org/10.1016/j.jhydrol.2015.07.039>, 2015.
- 482 Evenson, G. R., Golden, H. E., Lane, C. R., and D'Amico, E.: An improved representation of geographically isolated
483 wetlands in a watershed-scale hydrologic model, *Hydrological Processes*, 2016.
- 484 Gleason, R. A., Tangen, B. A., Laubhan, M. K., Kermes, K. E., and Euliss Jr, N. H.: Estimating water storage
485 capacity of existing and potentially restorable wetland depressions in a subbasin of the Red River of the North,
486 U.S. Geological Survey Open-File Report 2007-1159., 36, 2007.
- 487 Gleason, R. A., Laubhan, M. K., Tangen, B. A., and Kermes, K. E.: Ecosystem services derived from wetland
488 conservation practices in the United States Prairie Pothole Region with an emphasis on the US Department of
489 Agriculture Conservation Reserve and Wetlands Reserve Programs, 2008.



- 490 Golden, H. E., Lane, C. R., Amatya, D. M., Bandilla, K. W., Kiperwas, H. R., Knightes, C. D., and Ssegane, H.:
 491 Hydrologic connectivity between geographically isolated wetlands and surface water systems: A review of
 492 select modeling methods, *Environ. Modell. Softw.*, 53, 190-206, 10.1016/j.envsoft.2013.12.004, 2014.
- 493 Golden, H. E., Creed, I., Ali, G., Basu, N., Neff, B., Rains, M., McLaughlin, D., Alexander, L., Ameli, A.,
 494 Christensen, J., Evenson, G., Jones, C., Lane, C., and Lang, M.: Scientific tools for integrating geographically
 495 isolated wetlands into land management decisions, *Frontiers in Ecology and the Environment* (in review),
 496 2016.
- 497 Hayashi, M., van der Kamp, G., and Rudolph, D. L.: Water and solute transfer between a prairie wetland and
 498 adjacent uplands, 1. Water balance, *Journal of Hydrology*, 207, 42-55, [http://dx.doi.org/10.1016/S0022-](http://dx.doi.org/10.1016/S0022-1694(98)00098-5)
 499 [1694\(98\)00098-5](http://dx.doi.org/10.1016/S0022-1694(98)00098-5), 1998.
- 500 Hayashi, M., and Van der Kamp, G.: Simple equations to represent the volume–area–depth relations of shallow
 501 wetlands in small topographic depressions, *Journal of Hydrology*, 237, 74-85, 2000.
- 502 Hayashi, M., van der Kamp, G., and Rosenberry, D. O.: Hydrology of Prairie Wetlands: Understanding the
 503 Integrated Surface-Water and Groundwater Processes, *Wetlands*, 1-18, 10.1007/s13157-016-0797-9, 2016.
- 504 Huang, C., Peng, Y., Lang, M., Yeo, I. Y., and McCarty, G.: Wetland inundation mapping and change monitoring
 505 using Landsat and airborne LiDAR data, *Remote Sensing of Environment*, 141, 231-242, 2014.
- 506 Huang, S., Dahal, D., Young, C., Chander, G., and Liu, S.: Integration of Palmer Drought Severity Index and remote
 507 sensing data to simulate wetland water surface from 1910 to 2009 in Cottonwood Lake area, North Dakota,
 508 *Remote Sensing of Environment*, 115, 3377-3389, 2011a.
- 509 Huang, S., Young, C., Feng, M., Heidemann, K., Cushing, M., Mushet, D. M., and Liu, S.: Demonstration of a
 510 conceptual model for using LiDAR to improve the estimation of floodwater mitigation potential of Prairie
 511 Pothole Region wetlands, *Journal of Hydrology*, 405, 417-426, 2011b.
- 512 Hubbard, D. E., and Linder, R. L.: Spring runoff retention in prairie pothole wetlands, *Journal of Soil & Water
 513 Conservation*, 41, 122-125, 1986.
- 514 Jin, S., Yang, L., Danielson, P., Homer, C., Fry, J., and Xian, G.: A comprehensive change detection method for
 515 updating the national land cover database to circa 2011, *Remote Sensing of Environment*, 132, 159-175, 2013.
- 516 Johnston, C. A.: Wetland losses due to row crop expansion in the dakota prairie pothole region, *Wetlands*, 33, 175-
 517 182, 10.1007/s13157-012-0365-x, 2013.
- 518 Keddy, P. A.: *Wetland ecology: principles and conservation*, Cambridge University Press, 2010.
- 519 Kweon, I. S., and Kanade, T.: Extracting topographic terrain features from elevation maps, *CVGIP: Image
 520 Understanding*, 59, 171-182, 10.1006/ciun.1994.1011, 1994.
- 521 Lane, C. R., and D'Amico, E.: Identification of Putative Geographically Isolated Wetlands of the Conterminous
 522 United States, *JAWRA Journal of the American Water Resources Association*, n/a-n/a, 10.1111/1752-
 523 1688.12421, 2016.
- 524 Lang, M., and McCarty, G.: Lidar intensity for improved detection of inundation below the forest canopy, *Wetlands*,
 525 29, 1166-1178, 10.1672/08-197.1, 2009.
- 526 Lindsay, J. B., and Creed, I. F.: Distinguishing actual and artefact depressions in digital elevation data, *Computers
 527 and Geosciences*, 32, 1192-1204, 10.1016/j.cageo.2005.11.002, 2006.
- 528 McCauley, L., and Anteau, M.: Generating Nested Wetland Catchments with Readily-Available Digital Elevation
 529 Data May Improve Evaluations of Land-Use Change on Wetlands, *Wetlands*, 1-10, 10.1007/s13157-014-0571-
 530 9, 2014.
- 531 Metz, M., Mitasova, H., and Harmon, R.: Efficient extraction of drainage networks from massive, radar-based
 532 elevation models with least cost path search, *Hydrology and Earth System Sciences*, 15, 667-678, 2011.
- 533 Miller, M. W., and Nudds, T. D.: Prairie landscape change and flooding in the Mississippi River Valley,
 534 *Conservation Biology*, 10, 847-853, 1996.
- 535 Minke, A. G. N.: *Estimating water storage of prairie pothole wetlands*, University of Saskatchewan, 2009.
- 536 Mushet, D. M., and Euliss, N. H.: The Cottonwood Lake study area, a long-term wetland ecosystem monitoring site,
 537 *US Geological Survey* 2327-6932, 2012.
- 538 O'Callaghan, J. F., and Mark, D. M.: The extraction of drainage networks from digital elevation data, *Computer
 539 vision, graphics, and image processing*, 28, 323-344, 1984.
- 540 Oslund, F. T., Johnson, R. R., and Hertel, D. R.: Assessing Wetland Changes in the Prairie Pothole Region of
 541 Minnesota From 1980 to 2007, *Journal of Fish and Wildlife Management*, 1, 131-135, 10.3996/122009-
 542 JFWM-027, 2010.



- 543 Rains, M. C., Leibowitz, S. G., Cohen, M. J., Creed, I. F., Golden, H. E., Jawitz, J. W., Kalla, P., Lane, C. R., Lang,
 544 M. W., and McLaughlin, D. L.: Geographically isolated wetlands are part of the hydrological landscape,
 545 Hydrological Processes, 30, 153-160, 10.1002/hyp.10610, 2016.
- 546 Rover, J., and Mushet, D. M.: 16 Mapping Wetlands and Surface Water in the Prairie Pothole Region of North
 547 America, Remote Sensing of Wetlands: Applications and Advances, 347, 2015.
- 548 Shaw, D. A., Vanderkamp, G., Conly, F. M., Pietroniro, A., and Martz, L.: The fill–spill hydrology of Prairie
 549 wetland complexes during drought and deluge, Hydrological Processes, 26, 3147-3156, 2012.
- 550 Shaw, D. A., Pietroniro, A., and Martz, L.: Topographic analysis for the prairie pothole region of Western Canada,
 551 Hydrological Processes, 27, 3105-3114, 2013.
- 552 Sloan, C. E.: Ground-water hydrology of prairie potholes in North Dakota, Professional Paper 585-C, U.S.
 553 Government Printing Office Washington, D.C., USA, 1972.
- 554 Stanislawski, L. V.: Feature pruning by upstream drainage area to support automated generalization of the United
 555 States National Hydrography Dataset, Computers, Environment and Urban Systems, 33, 325-333,
 556 <http://dx.doi.org/10.1016/j.compenvurbsys.2009.07.004>, 2009.
- 557 Steen, V., Skagen, S. K., and Noon, B. R.: Vulnerability of Breeding Waterbirds to Climate Change in the Prairie
 558 Pothole Region, U.S.A, PLoS ONE, 9, e96747, 10.1371/journal.pone.0096747, 2014.
- 559 Stein, A., Pebesma, E., Heuvelink, G., Melles, S. J., Jones, N. E., Schmidt, B., and Rayfield, B.: Spatial Statistics
 560 2011: Mapping Global Change A least-cost path approach to stream delineation using lakes as patches and a
 561 digital elevation model as the cost surface, Procedia Environmental Sciences, 7, 240-245,
 562 <http://dx.doi.org/10.1016/j.proenv.2011.07.042>, 2011.
- 563 Tiner, R.: Geographically isolated wetlands of the United States, Wetlands, 23, 494-516, 10.1672/0277-
 564 5212(2003)023[0494:GIWOTU]2.0.CO;2, 2003.
- 565 Tiner, R. W.: NWI maps: what they tell us, National Wetlands Newsletter, 19, 7-12, 1997.
- 566 Todhunter, P. E., and Rundquist, B. C.: Terminal lake flooding and wetland expansion in Nelson County, North
 567 Dakota, Phys. Geogr., 25, 68-85, 2004.
- 568 Tromp-van Meerveld, H. J., and McDonnell, J. J.: Threshold relations in subsurface stormflow: 2. The fill and spill
 569 hypothesis, Water Resources Research, 42, n/a-n/a, 10.1029/2004WR003800, 2006a.
- 570 Tromp-van Meerveld, H. J., and McDonnell, J. J.: Threshold relations in subsurface stormflow: 1. A 147-storm
 571 analysis of the Panola hillslope, Water Resources Research, 42, n/a-n/a, 10.1029/2004WR003778, 2006b.
- 572 U.S. EPA: Connectivity and effects of streams and wetlands on downstream waters: A review and synthesis of the
 573 scientific evidence, U.S. Environmental Protection Agency, Washington, D.C., 2015.
- 574 Vanderhoof, M., Alexander, L., and Todd, M. J.: Temporal and spatial patterns of wetland extent influence
 575 variability of surface water connectivity in the Prairie Pothole Region, United States, Landscape Ecology, 31,
 576 805–824, 10.1007/s10980-015-0290-5, 2016.
- 577 Wang, C.-K., and Philpot, W. D.: Using airborne bathymetric lidar to detect bottom type variation in shallow waters,
 578 Remote Sensing of Environment, 106, 123-135, 2007.
- 579 Wang, L., and Liu, H.: An efficient method for identifying and filling surface depressions in digital elevation models
 580 for hydrologic analysis and modelling, International Journal of Geographical Information Science, 20, 193-
 581 213, 2006.
- 582 Watmough, M. D., and Schmoll, M. J.: Environment Canada's Prairie & Northern Region Habitat Monitoring
 583 Program, Phase II: Recent Habitat Trends in the Prairie Habitat Joint Venture, Canadian Wildlife Service,
 584 2007.
- 585 Winter, T.: Hydrologic studies of wetlands in the northern prairie, in: Northern Prairie Wetlands, edited by: Van Der
 586 Valk, A. G., Iowa-State University Press, Ames, IA, 1989.
- 587 Winter, T. C., and Rosenberry, D. O.: The interaction of ground water with prairie pothole wetlands in the
 588 Cottonwood Lake area, east-central North Dakota, 1979-1990, Wetlands, 15, 193-211, 1995.
- 589 Wu, Q., Lane, C., and Liu, H.: An Effective Method for Detecting Potential Woodland Vernal Pools Using High-
 590 Resolution LiDAR Data and Aerial Imagery, Remote Sensing, 6, 11444-11467, 10.3390/rs61111444, 2014.
- 591 Wu, Q., Liu, H., Wang, S., Yu, B., Beck, R., and Hinkel, K.: A localized contour tree method for deriving geometric
 592 and topological properties of complex surface depressions based on high-resolution topographical data,
 593 International Journal of Geographical Information Science, 29, 2041-2060, 10.1080/13658816.2015.1038719,
 594 2015.
- 595 Wu, Q., and Lane, C. R.: Delineation and Quantification of Wetland Depressions in the Prairie Pothole Region of
 596 North Dakota, Wetlands, 36, 215-227, 10.1007/s13157-015-0731-6, 2016.



- 597 Zhang, B., Schwartz, F. W., and Liu, G.: Systematics in the size structure of prairie pothole lakes through drought
598 and deluge, *Water Resources Research*, 45, 2009.
- 599 Zhao, L., and Wu, F.: Simulation of Runoff Hydrograph on Soil Surfaces with Different Microtopography Using a
600 Travel Time Method at the Plot Scale, *PloS one*, 10, e0130794, 2015.
- 601 Zhu, X.: *GIS for Environmental Applications: A Practical Approach*, Routledge, 2016.
- 602



603 **Table 1.** Summary statistics of the National Wetlands Inventory (NWI) for the Pipestem subbasin, North Dakota.

Wetland type	Count	Min (m ²)	Max (m ²)	Median (m ²)	Sum (m ²)	Percentage
Freshwater Emergent Wetland	31,046	500	3,105,826	1,770	241,733,542	86.5%
Freshwater Forested/Shrub Wetland	108	548	343,950	2,572	1,175,739	0.4%
Freshwater Pond	760	533	719,339	1,772	14,719,510	5.3%
Lake	50	3,746	9,410,427	188,600	21,055,438	7.5%
Riverine	52	634	429,838	4,021	811,488	0.3%
Total (all polygons)	32,016	500	9,410,427	1,778	279,495,717	100.0%

604



605 **Table 2.** Summary statistics of NWI wetland polygons and inundation polygons derived from LiDAR intensity data.

Type	Count	Min (m ²)	Max (m ²)	Mean (m ²)	Median (m ²)	Sum (m ²)
NWI polygons	32,016	500	9,410,427	8,728	1,778	279,495,717
Inundation polygons	15,784	500	7,348,000	17,650	1,825	278,523,863
Dried NWI polygons	18,957	500	112,100	2,299	1,212	43,574,627

606



607 **Table 3.** Summary statistics of 33,241 wetland depressions and catchments derived from LiDAR DEM.

Type	Min	Max	Mean	Median	Sum
Depression area (m ²)	1008	20,030,000	16,590	2592	554,506,299
Catchment area (m ²)	1818	57,900,000	82,710	25,780	2,770,116,549
Depression volume (m ³)	1	153,000,000	23,420	420	782,886,383
Proportion of depression area to catchment area (%)	0.04	83.72	16.59	14.31	20.06

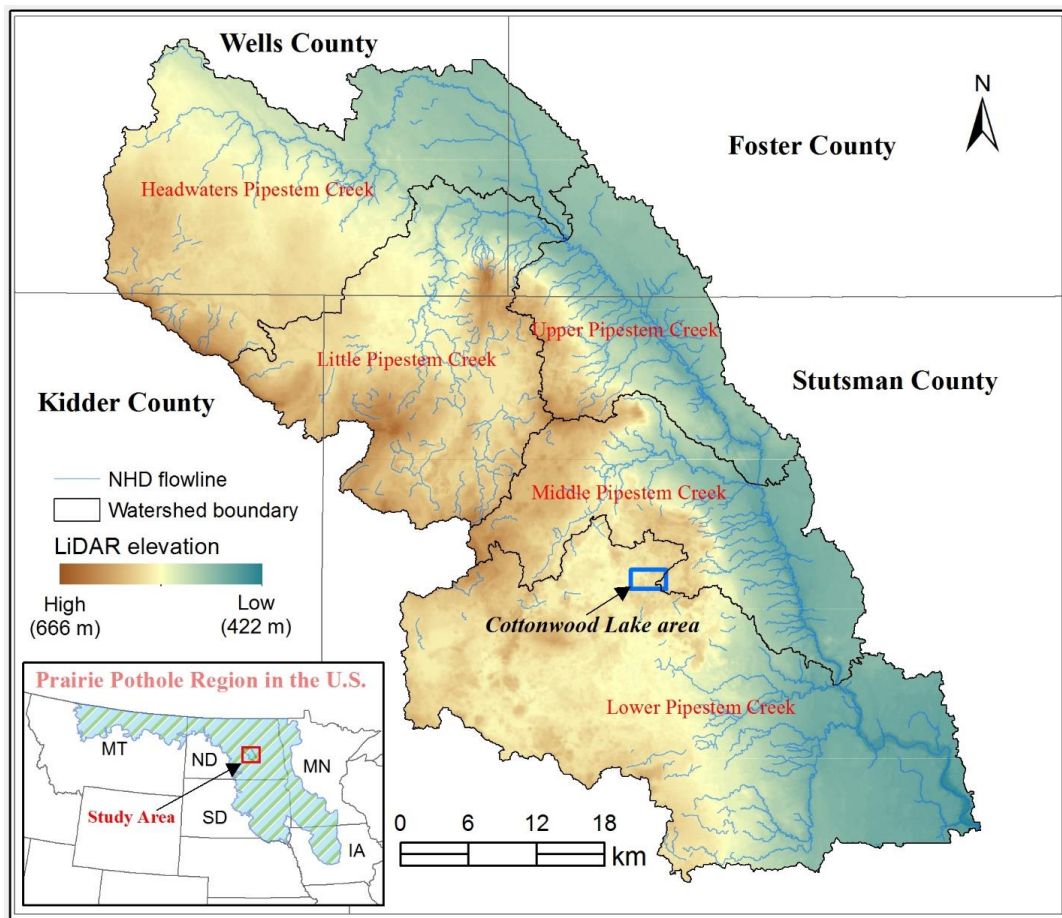
608



609 **Table 4.** Summary statistics of wetland depression ponding depth, NHD flowlines, connectivity length, and
610 elevation difference.

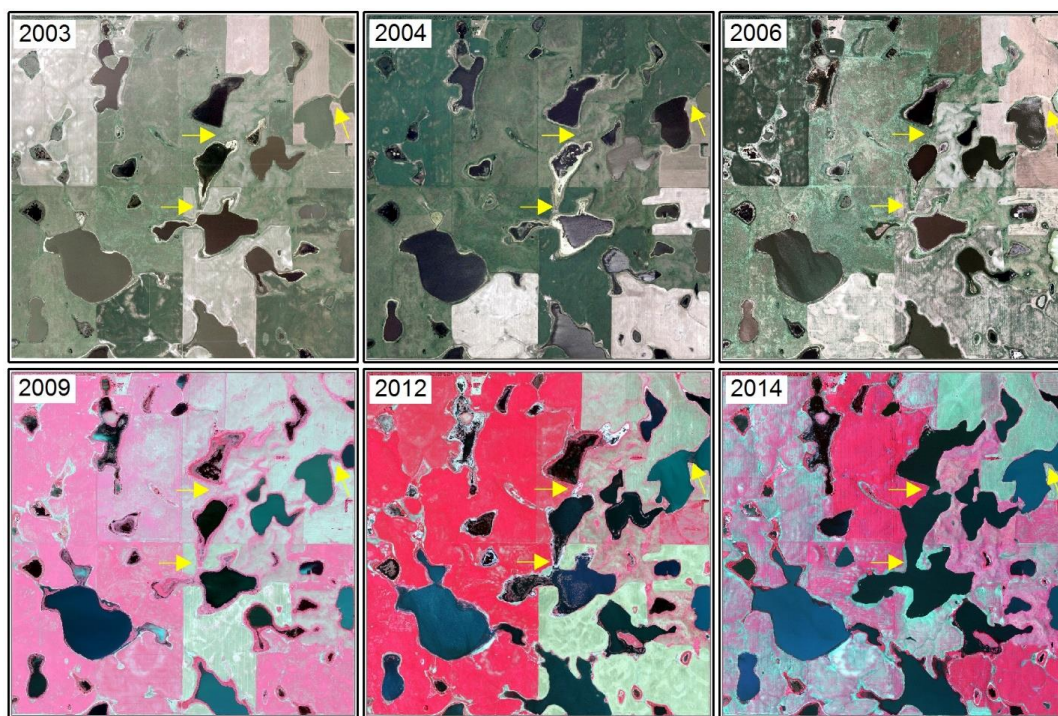
Type	Count	Min (m)	Max (m)	Mean (m)	Median (m)	Sum (m)
Ponding depth	33,241	0.01	7.64	0.23	0.16	NA
NHD flowlines	1840	3.89	15,530	762	317	1,402,226
Connectivity length	41,449	1.5	4,658	138	83	5,014,495
Elevation difference	41,449	0.01	70.89	2.14	0.89	NA

611



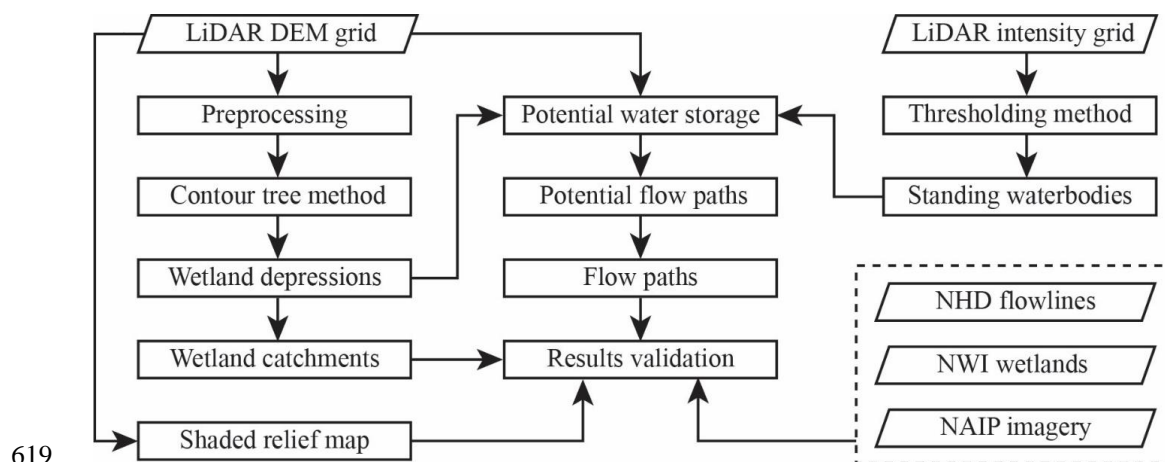
612

613 **Figure 1.** Location of the Pipestem subbasin within the Prairie Pothole Region of North Dakota.



614

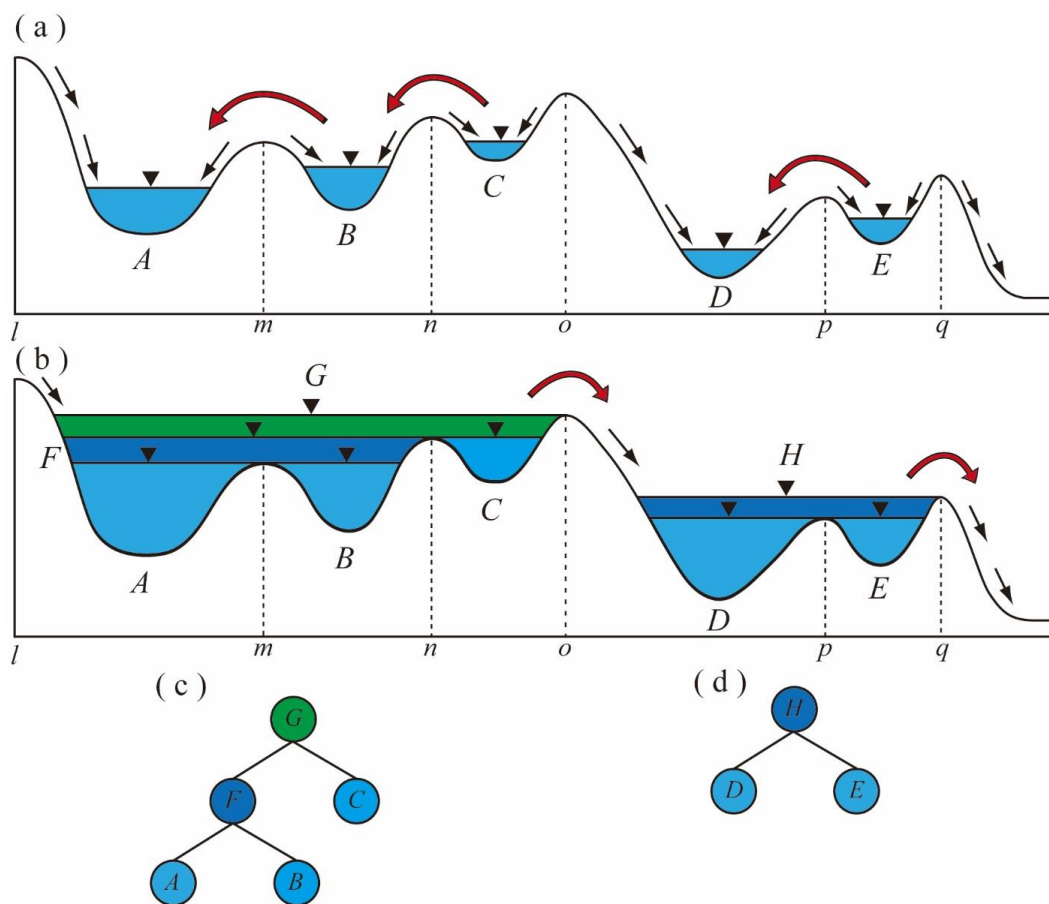
615 **Figure 2.** Examples of the National Agriculture Imagery Program (NAIP) aerial imagery in the Prairie Pothole
616 Region of North Dakota illustrate the dynamic nature of prairie pothole wetlands under various dry and wet
617 conditions. The yellow arrows highlight locations where filling-spilling-merging dynamics occurred (imagery
618 location: 99°8'34.454" W, 47°1'23.519" N).



619

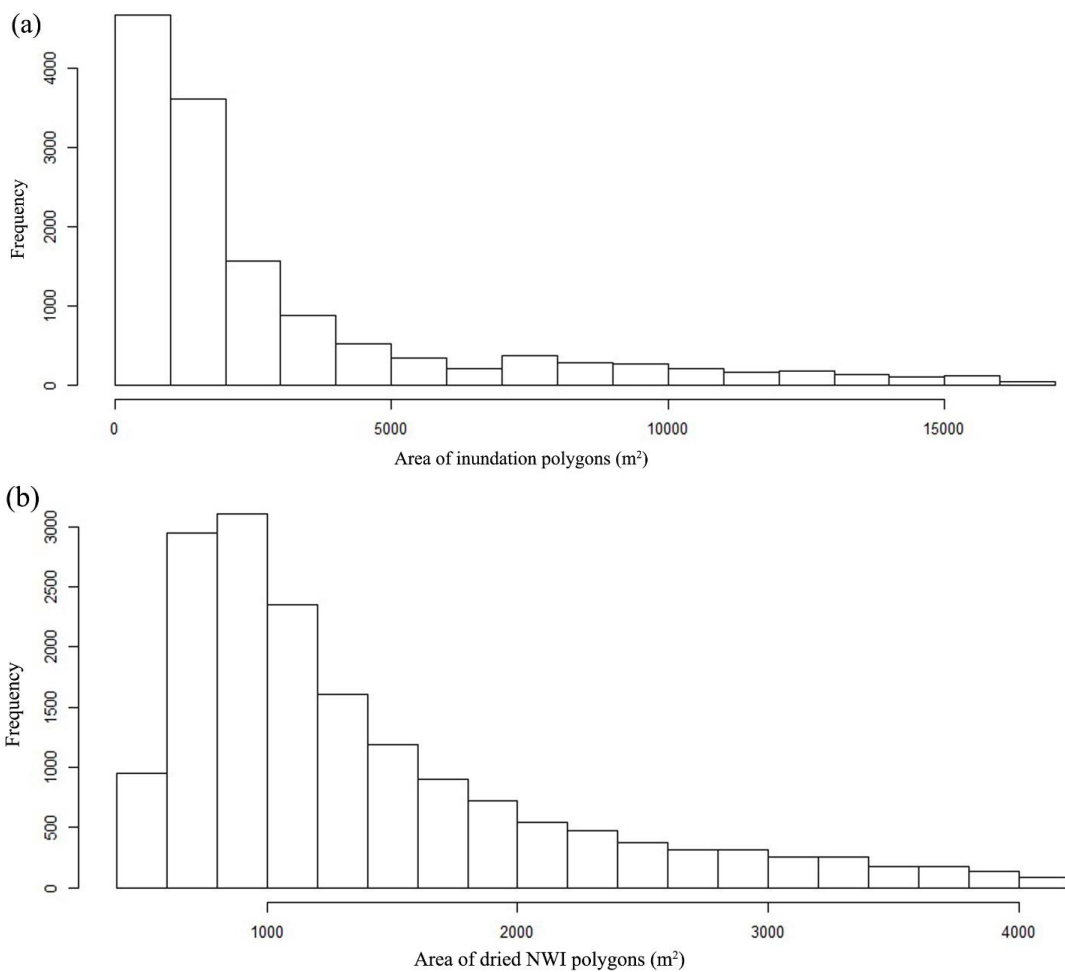
620

Figure 3. Flowchart of the methodology for delineating wetland catchments and flow paths.



621

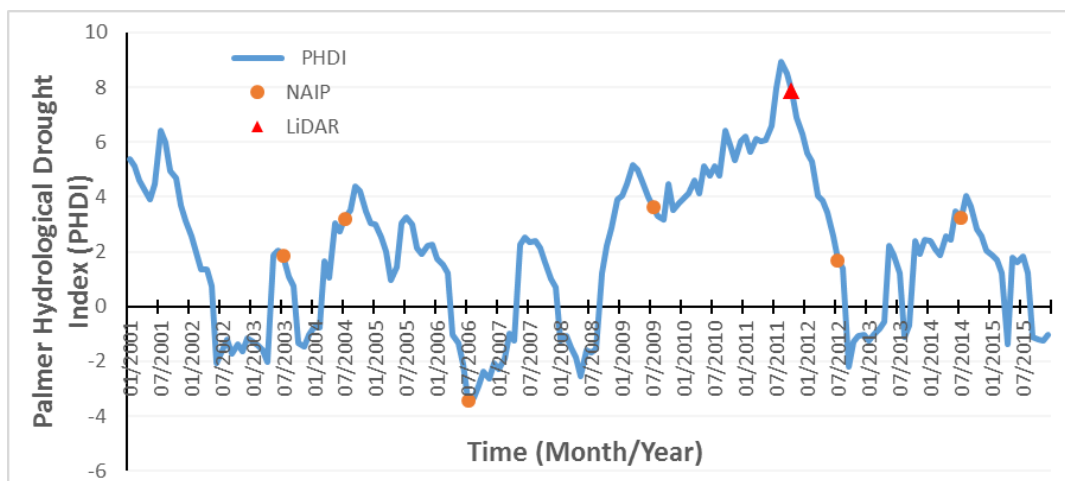
622 **Figure 4.** Illustration of the filling-merging-spilling dynamics of wetland depressions: (a) first-level depressions; (b)
 623 nested hierarchical structure of depressions under fully-filled condition; (c) corresponding contour tree
 624 representation of the composite wetland depression (left) in (a); and (d) corresponding contour tree representation of
 625 the composite wetland depression (right) in (a). Different color of nodes in the tree represents different portions of
 626 the composite depression in (a): light blue (first-level), dark blue (second-level), and green (third-level).



627

628

629 **Figure 5.** Histograms of inundation and NWI wetland polygons. (a) Inundation objects derived from LiDAR
630 intensity data; (b) dried NWI wetland polygons not intersecting inundation objects.



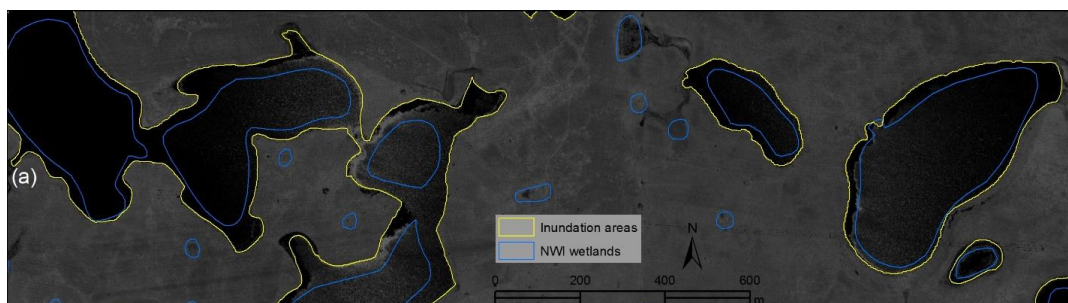
631

632

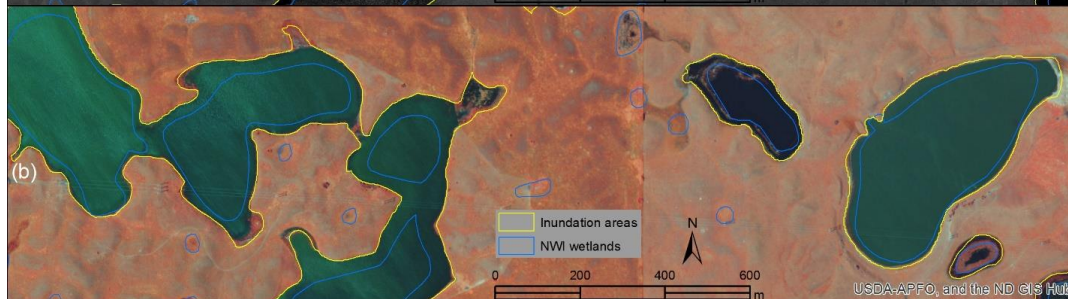
Figure 6. Palmer Hydrological Drought Index (PHDI) of the Pipestem subbasin (2001-2015).



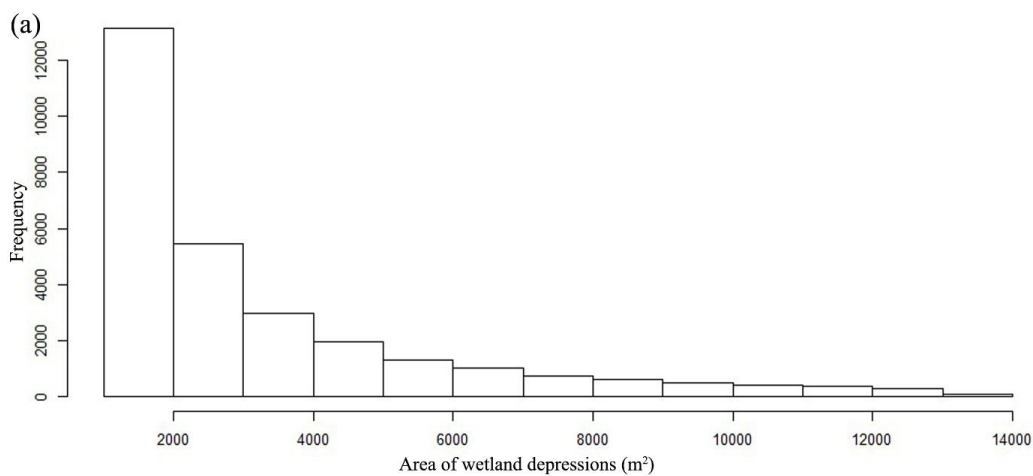
633



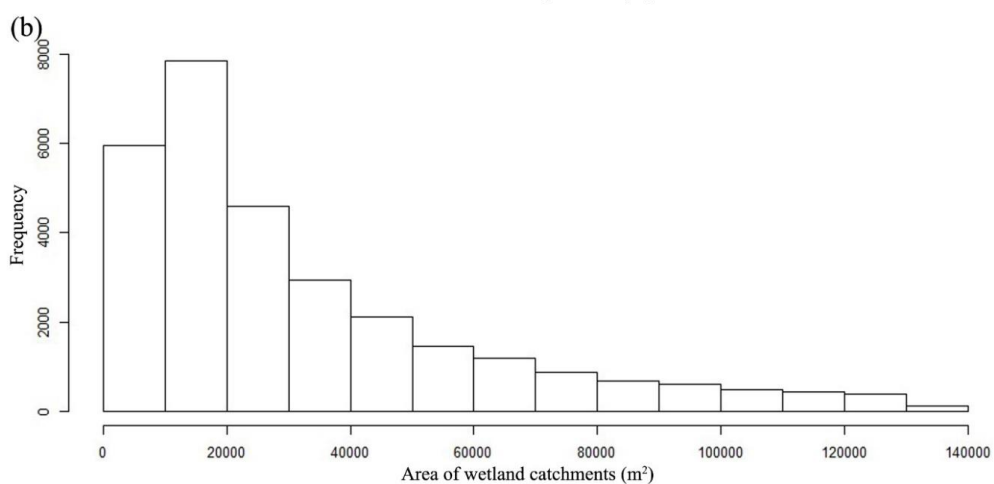
634



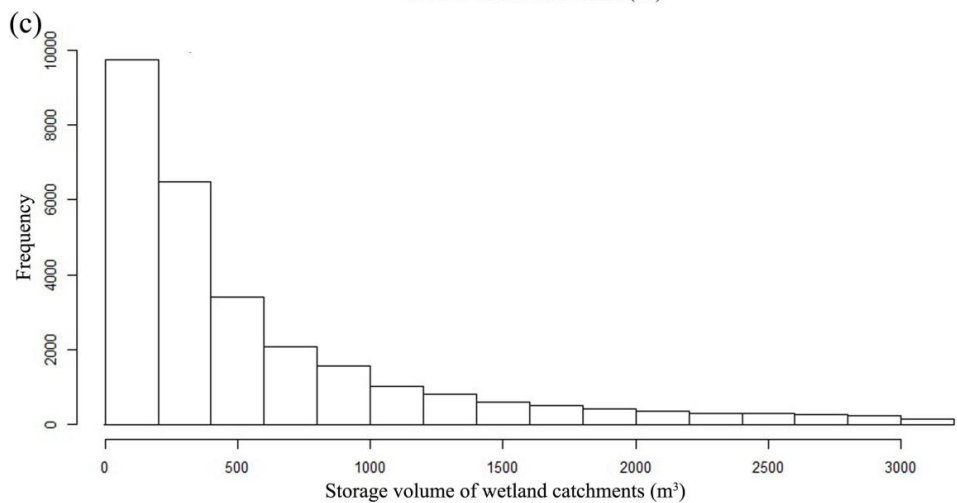
635 **Figure 7.** Comparison between inundation areas (derived from LiDAR intensity data) and NWI wetland polygons
636 (image location: 99°9'53.9" W, 47°3'34.474" N). (a) Inundation areas and NWI wetlands overlaid on LiDAR
637 intensity image; and (b) inundation areas and NWI wetlands overlaid on color infrared aerial photograph (2009).



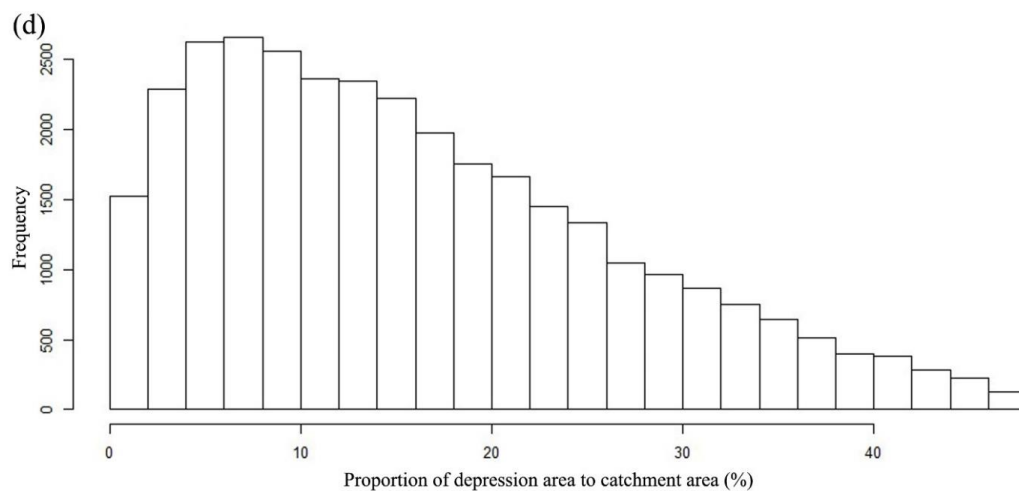
638



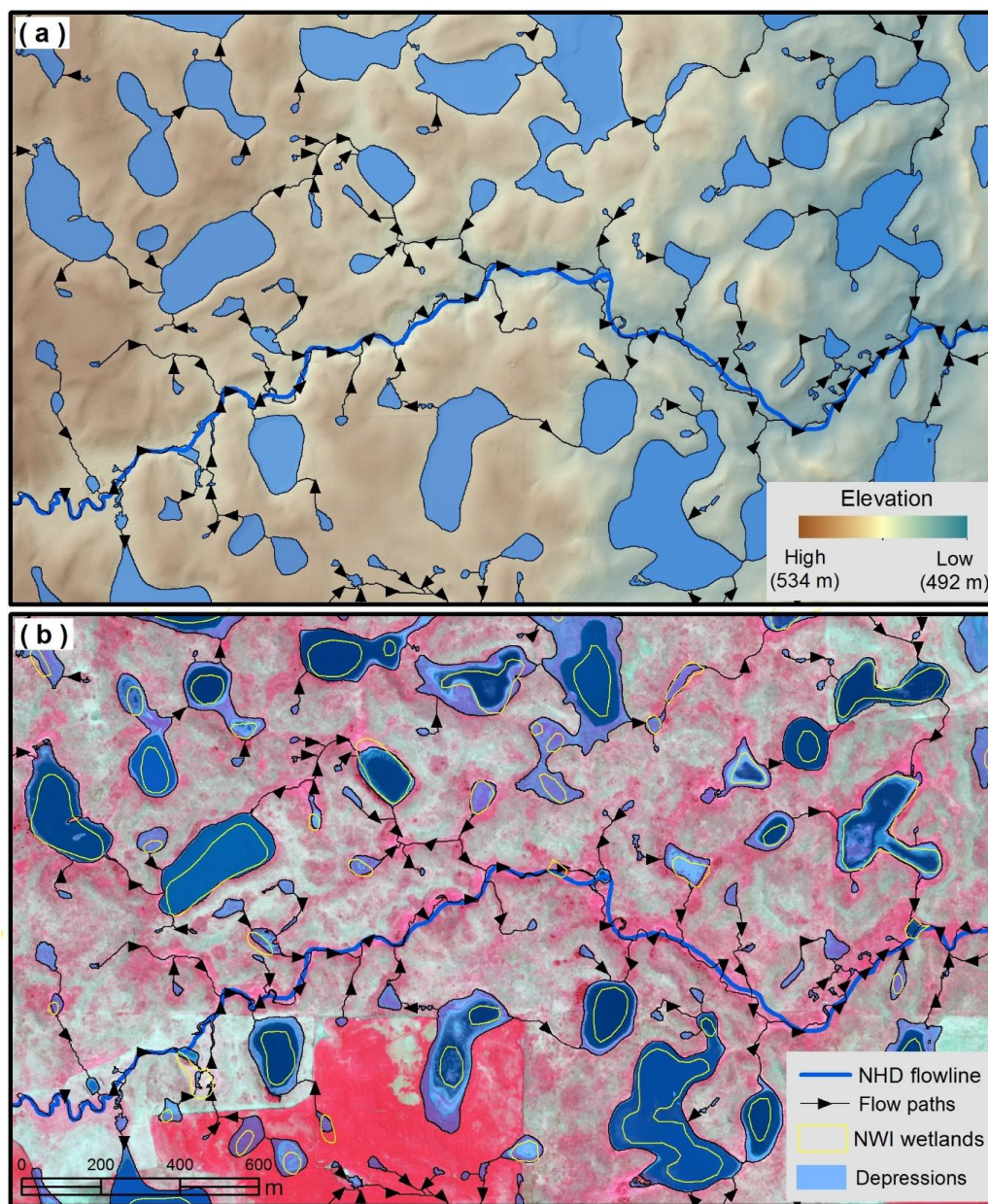
639



640

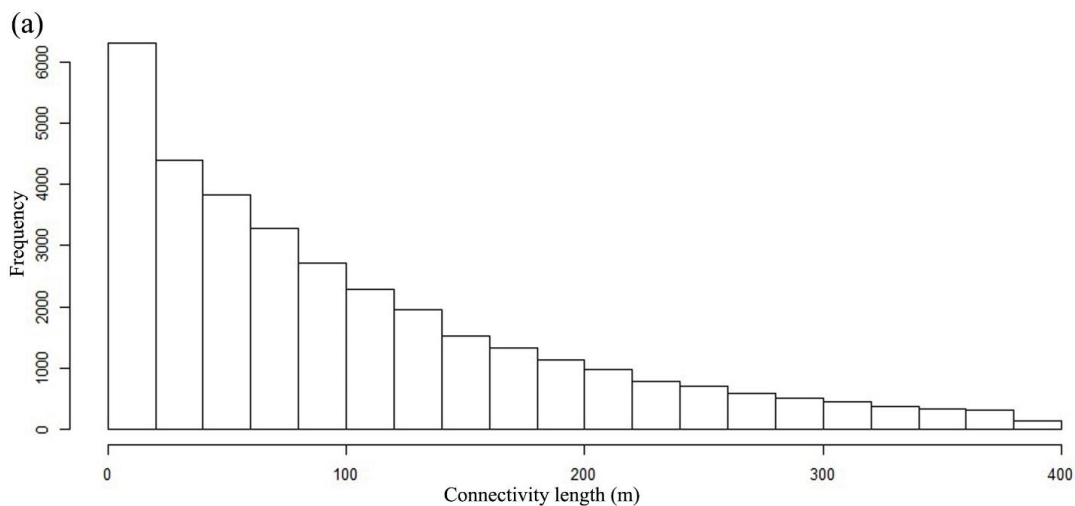


641
642 **Figure 8.** Histogram of wetland depressions and catchments. (a) Wetland depressions; (b) wetland catchments; (c)
643 potential storage capacity; and (d) proportion of depression area to catchment area.

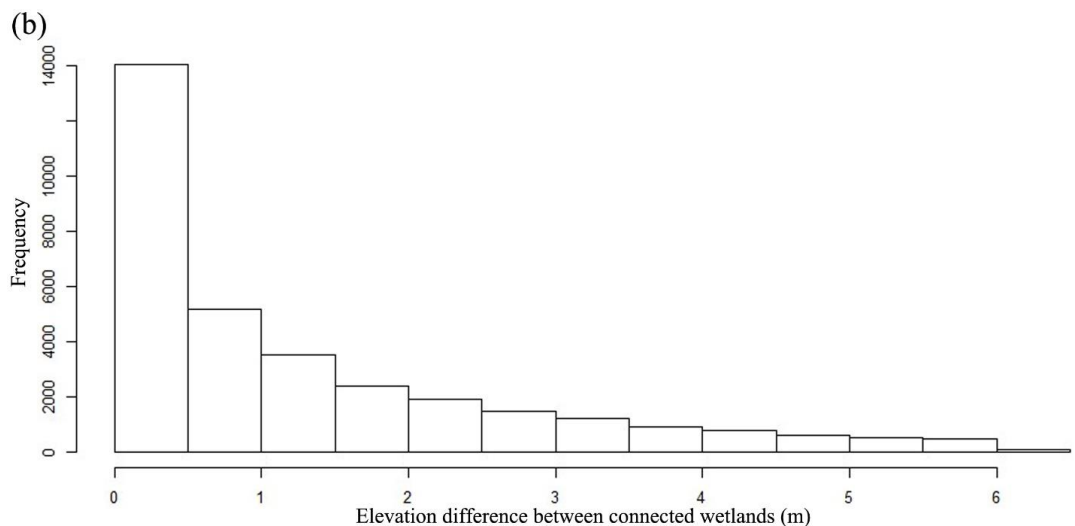


644

645 **Figure 9.** Examples of LiDAR-derived wetland depressions and flow paths in the Pipestem subbasin (image
646 location: 98°59'48.82" W, 47°1'32.679" N). (a) Wetland depressions and flow paths overlaid on LiDAR shaded
647 relief map; and (b) NWI polygons, wetland depressions and flow paths overlaid on color infrared aerial photograph
648 (2012).



649



650

651 **Figure 10.** Histogram of wetland connectivity. (a) Connectivity lengths; and (b) elevation differences between
652 connected wetlands.